Optics & Laser Technology 181 (2025) 111779

Contents lists available at ScienceDirect

Optics and Laser Technology

journal homepage: www.elsevier.com/locate/optlastec

Full length article

Ad hoc calibration of interferometric system for measuring nanometer-scale displacements induced by laser ultrasound

Younggue Kim [a], Taeil Yoon [b], Byeongha Lee [a,*]

[a] School of Electrical Engineering and Computer Science, Gwangju Institute of Science and Technology (GIST), 123 Cheomdangwagi-ro, Buk-gu, Gwangju 61005, Republic of Korea

[b] The Institute of Basic Science, Korea University, 145 Anam-Ro, Seongbuk-Gu, Seoul 02841, Korea

ARTICLE INFO

Keywords:
Interferometry
Displacement measurement
Thickness measurement
Laser Ultrasound (LUS)
Ultrasound detection
Fiber optic

ABSTRACT

Laser Ultrasound (LUS) is commonly used in many fields including thickness measurement and defect inspection. In a conventional LUS system, a piezo-based transducer (PZT) is generally used for detecting the ultrasound echo waves, which requires direct contact with a specimen and thus prolongs measurement time when any lateral scanning is necessary. We present a novel non-contact interferometric system based on a 3 × 3 optical fiber coupler. Even though the 3 × 3 interferometric system works stably at any operating point and allows quantitative measurements, it is generally known that careful calibration is necessary before main measurements. Experimentally, it was observed that the surface displacement, induced by the ultrasound wave of LUS, of a cornea phantom was so minute that averaging was necessary. In this study, we discovered that by using the multiple data sets acquired for averaging, we could obtain the system ad hoc characteristic ellipse without performing the conventional calibration process. Furthermore, by utilizing coherent average we could extract the displacement with a 0.14 nm sensitivity. We could also measure the thickness variation, induced by ocular pressure, of the cornea phantom with a resolution of 4.3 μm by measuring the time of a round trip of the ultrasound wave. This straightforward system, composed solely of a 3 × 3 coupler, is expected to promise a compact and efficient solution to diverse applications.

1. Introduction

Laser Ultrasound (LUS) technology has found applications primarily in industrial fields for measuring thickness or inspecting defects inside or on the surface of a specimen [1,2]. Initially, ultrasound wave was generated at the specimen surface using a laser pulse, and the echo waves reflected from the target inside the specimen were detected with a piezo-based transducer (PZT). However, using a PZT led to a prolonged measurement time because it could not move quickly due to the contact with the specimen. For a biological specimen, the contact itself could give some discomfort and fundamental restrictions. In response, a non-contact method utilizing a laser-based detector instead of PZT was proposed [3–8].

At present, optical interferometers serve as the tools for prevalent non-contact measurements. Optical interferometers offer the advantage of measuring minute displacements without making physical contact with the specimen. They have been utilized for detecting cracks inside airplanes or measuring the thicknesses of steel plates [7]. Particularly, optical fiber-based interferometers have the added advantage of being easier to configure than free space ones. However, they have the drawback of being highly sensitive to initial phase or operating point drift, which could be affected by building vibration, temperature fluctuation, and atmospheric pressure change. To address this sensitivity and stability issues, various systems have been proposed, including the installation of additional modulators [9–14]. Yet, these solutions came with the drawbacks of complexity and high cost.

To overcome the initial phase problem and to achieve the measurement of nanometer-scale displacement, the optical interferometer based on a 3 × 3 optical fiber coupler has been proposed. The most popular interferometer is based on a 2 × 2 coupler, which gives two interference signals having the intrinsic phase difference of 180 degrees. Therefore, for a small displacement, both signals show the same response, just with opposite signs, being sensitive to the initial phase or operating point of the system. One of the best ways of getting the phase information from an interferometer, as has been well known, is utilizing the I (in-phase) and Q (quadrature phase) signals. Since they are 90 degrees out of phase

* Corresponding author.
E-mail addresses: youngguekim92@gm.gist.ac.kr (Y. Kim), taeil021@gist.ac.kr (T. Yoon), leebh@gist.ac.kr (B. Lee).

https://doi.org/10.1016/j.optlastec.2024.111779
Received 26 July 2024; Received in revised form 5 September 2024; Accepted 9 September 2024
Available online 16 September 2024

with each other, the small phase information can be extracted without being affected by the drift of operating point or initial phase of the system.

Fortunately, in the interferometer based on a 3 × 3 coupler, the three output interference signals have intrinsic phase differences of around 120 degrees with each other. When any two signals are plotted simultaneously, the Lissajous curve is formed in an ellipse. The inclination angle of the ellipse is mainly due to the intrinsic phase difference. Through curve fitting, the parameters of the ellipse, called the characteristic ellipse of the system, are obtained and used for calculating the *IQ* signal pair [15–17]. However, the characteristic ellipse itself is affected by unintentional variations in the system parameters, including the coupling ratio of the coupler and the reflectivity on the specimen surface. Usually, the characteristic ellipse is obtained or constructed before the main measurement by driving a PZT in the reference arm. It has been reported that at least $\pi/4$ phase fraction of an ellipse is necessary for making a curve fit [18]. Therefore, when the measurement is made while scanning the surface laterally or the curvature of the surface is changed during the measurement, the parameters of the ellipse need to be recalibrated to maintain the same level of accuracy.

In this work, we propose the optical interferometric system that is based on a 3 × 3 optical fiber coupler but does not need the prior PZT driving for ellipse calibration. When the displacement under measurement is very small, average is generally utilized to reduce noise, which requires several measurements at the same condition. Fortunately, it was experimentally observed that the multiple measurements could provide the parameters of the characteristic ellipse. By doing the average coherently, we could achieve the measurement of sub-nanometer displacements. Therefore, by averaging the multiple signals acquired under the same condition, we could get not only initial phase insensitive measurement but also high resolution.

To prove the concept, the surface displacements caused by the ultrasound waves of LUS on a cornea mimicking phantom were measured. By measuring the time of a round trip of ultrasound echo wave induced by LUS within the cornea phantom, the ocular pressure-induced cornea thickness variation was measured. Interestingly, however, the ocular pressure changed the characteristic ellipse, asking re-calibration at each pressure. Nevertheless, by utilizing the proposed scheme and coherent averaging, we were able to measure the nanometer-scale displacements at the surface of the cornea phantom driven by the ultrasound echo waves.

2. Method

2.1. Laser ultrasound (LUS)

In a LUS system, a short and strong laser pulse generates ultrasound waves on the surface of a specimen through the photoacoustic effect [1–8]. The ultrasound waves propagate into the specimen and are reflected at target objects located within the volume. The returned or echo ultrasound waves are then detected typically by a PZT at the surface. To address the issue of contact, this work measures surface displacement induced by ultrasound waves using optical interferometry. By analyzing the ultrasound echo waves, the thickness variation of a cornea phantom is calculated with respect to the ocular pressure applied to the cornea chamber.

2.2. Interferometer based on a 3 × 3 optical fiber coupler

The optical interferometer based on a 3 × 3 optical fiber coupler is implemented in a Mach-Zehnder configuration as depicted in Fig. 1. A continuous wave (CW) laser (SFL1550P, Thorlabs. Inc., Newton, NJ, USA) with a center wavelength of 1550 nm is split into a 99:1 ratio with a 1 × 2 optical fiber coupler. To cope with the specimen having low reflectivity, 99 percent of the beam is directed toward the sample arm with a circulator, while 1 percent to the reference arm. Such adjustment is convenient in the Mach-Zehnder configuration over the Michelson one [15]. The intensity of the beam in each arm is adjusted using a polarization controller and a neutral density filter to maximize the visibility of the interference. Subsequently, the interference signals are detected by two detectors (PDB460C, Thorlabs. Inc., Newton, NJ, USA), and the data is acquired using a digitizer (CSE123G2:YT1, Gage. Inc., Vitrek, LLC, USA). The detected interference signals are used to construct a Lissajous curve, which is then fitted to an ellipse. This ellipse provides the characteristic parameters of the system.

The two interference signals, denoted by I_x and I_y, of a 3 × 3 interferometer are generally given as [15,16,18]

$$I_x = h + a\cos\phi \tag{1}$$

$$I_y = k + b\cos(\phi + \delta) \tag{2}$$

$$\phi = 2k_0\Delta z + \phi_0 \tag{3}$$

Where, parameters h and k represent the DC levels of the interference signals, giving the center position of the characteristic ellipse. While, parameters a and b correspond to the AC amplitudes of signals, giving the aspect ratio of the ellipse. The intrinsic phase is denoted by δ. As a characteristic of the 3 × 3 coupler, the phase is around 120 degrees and affects the orientation of the principal axes of the ellipse. Lastly, ϕ denotes the phase angle of the interferogram. Where k_0 is a wavenumber of laser. It is proportional to the displacement Δz occurring in the sample arm, and shifted by the initial phase difference ϕ_0. Therefore, the applied displacement changes the phase ϕ in both Eqs. (1) and (2), and forms a fraction of an ellipse. As the phase amplitude increases, the

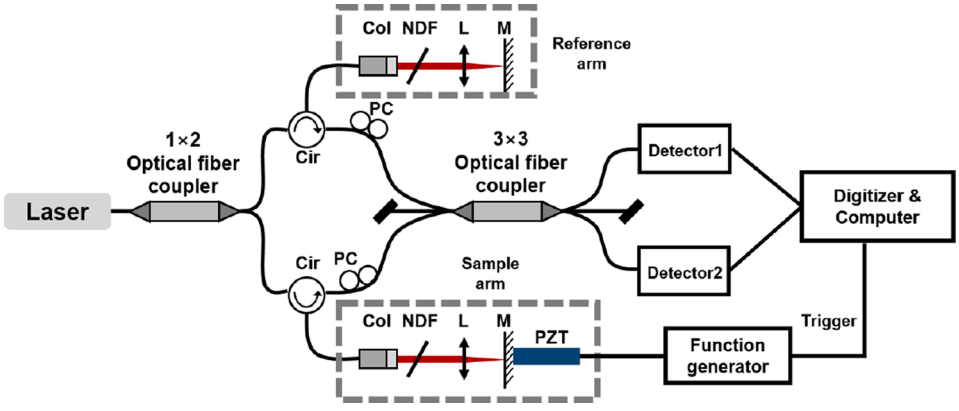

Fig. 1. Schematic of an interferometer based on a 3 × 3 optical fiber coupler. Cir: circulator, PC: polarization controller, L: lens, Col: collimator, NDF: neutral density filter, M: mirror, PZT: piezo-based transducer.

fraction increases. Consequently, the displacement corresponding to half the laser wavelength forms one complete cycle of the ellipse.

In general, the parameters not only h and k but a and b are affected by the amount of the light returned from the reference and sample arms. Even though the reference arm can be maintained stable, the beam returned from the sample arm depends heavily on the roughness and non-uniform reflectivity of the specimen surface. Thus, the four parameters (h, k, a, and b) fluctuate appreciably when the measurement point is scanned across the surface for a line or area measurement. The variation of the characteristic ellipse due to the change in the sample arm is experimentally tested and graphically presented in Fig. 2.

At first, with a PZT (PK2FSP2, Thorlabs. Inc., Newton, NJ, USA), the sample arm was sinusoidally oscillated at a frequency of 5 kHz with a V_{p-p} of 4 V. The measurement was made during a 16.32 ms for acquiring a single set of data, and total 10 sets were acquired with a time interval of 1 s in between. The Lissajous curve was plotted using these 10 sets of data and depicted in Fig. 2(a) (blue curve). We can see that all data points are well located along a closed line, which is fitted well to an ellipse as depicted with the red dotted curve. Then, the same measurement was repeated after slightly adjusting the neutral density filter to reduce the intensity of the beam returned from the sample arm. In Fig. 2 (a) (green curve), we can see that the data points are localized around a small ellipse, which is located far apart from the original curve. For better comparison, the second ellipse was enlarged in Fig. 2(b). While both ellipses appear similar in shape at first glance, closer examination reveals differences in center positions, sizes, orientations, and aspect ratios.

The fitting parameters of the first blue and the second green ellipses are presented in Table 1 [15,18]. With the fitted ellipse, the displacement Δz actuated in the sample arm was calculated using Eq. (3). In both cases, the applied displacements were properly reconstructed using their own fitting parameters, as shown in Fig. 2(c) and (d). However, when the green data in Fig. 2(b) was calculated using the fitting parameters of the previous blue ellipse in Fig. 2(a), significant distortion occurred, as seen in Fig. 2(e). This observation highlights the critical importance of ad hoc calibration of the characteristic ellipse of the system for ensuring reliable measurements.

Table 1
The fitting parameters of ellipses in Fig. 2.

	a	b	h	k	δ(rad)
Blue data	0.566	0.605	0.671	0.726	2.17
Green data	0.353	0.349	0.290	0.288	2.11

It is noteworthy that the curves in Fig. 2(a) and (b) appear as closed loops, forming complete ellipses. As mentioned earlier, to form one complete cycle of ellipse, a displacement of 775 nm, half the wavelength of the 1550 nm laser, is required. However, the calculated displacements in Fig. 2(c) and (d) are only 40 nm. In the next section, we will explain how to form the whole ellipse from such a small displacement amplitude of only 40 nm or less.

2.3. Small displacement measurement

In the previous section, it was confirmed that any two output signals of the 3 × 3 interferometer formed a fraction of the characteristic ellipse of the system. However, when the amplitude of the applied displacement was not big enough, it was impossible getting the whole ellipse from the measured data only. To obtain the whole ellipse from small but multiple fractions of ellipse, we conducted some experiments.

For experiment, the PZT in the sample arm was sinusoidally oscillated at a frequency of 25 kHz with a V_{p-p} of 1 V. A single data set was acquired over a 1.632 ms time period, and the corresponding Lissajous curve was plotted. Fig. 3(a) shows the acquired data along with the expected characteristic ellipse (red dotted line). We can see that the data bunch is in the shape of a silk cocoon, far from the shape of an ellipse. The same measurements were repeated several times, and the Lissajous curves were plotted with 10 sets Fig. 3(b), 20 sets Fig. 3(c), and 50 sets Fig. 3(d) of data. The time interval between successive sets was 1 s. Interestingly, as the number of data sets increased, the data bunches were distributed widely, enough for getting the whole characteristic ellipse. It is noted that the experiment was made at typical laboratory conditions, even on a regular optical table. This implies that the characteristic ellipse of the system can be obtained simply by repeating the

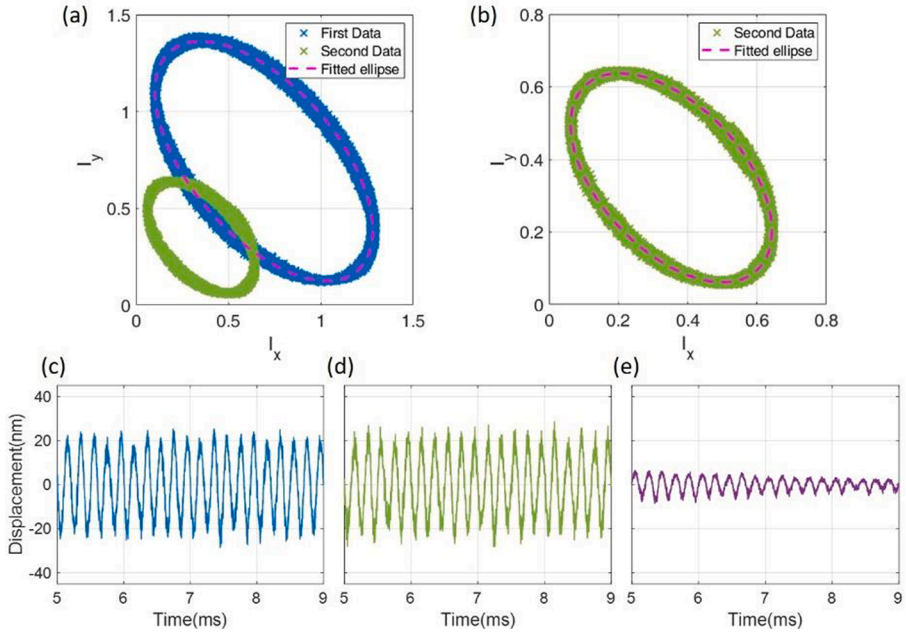

Fig. 2. Experimental verification of the characteristic ellipse being affected by the change in the sample arm. (a) Lissajous curve (blue) of a 5 kHz sinusoidal displacement, and the same one (green) but with a reduced sample arm intensity. (b) An enlarged figure of the green curve in (a). (c) The displacements in the blue data of (a), calculated with the blue ellipse parameters of (a). (d) The displacements in (b) calculated with the ellipse parameters of (b). (e) The displacements in data (b) but calculated with the blue ellipse parameters in (a).

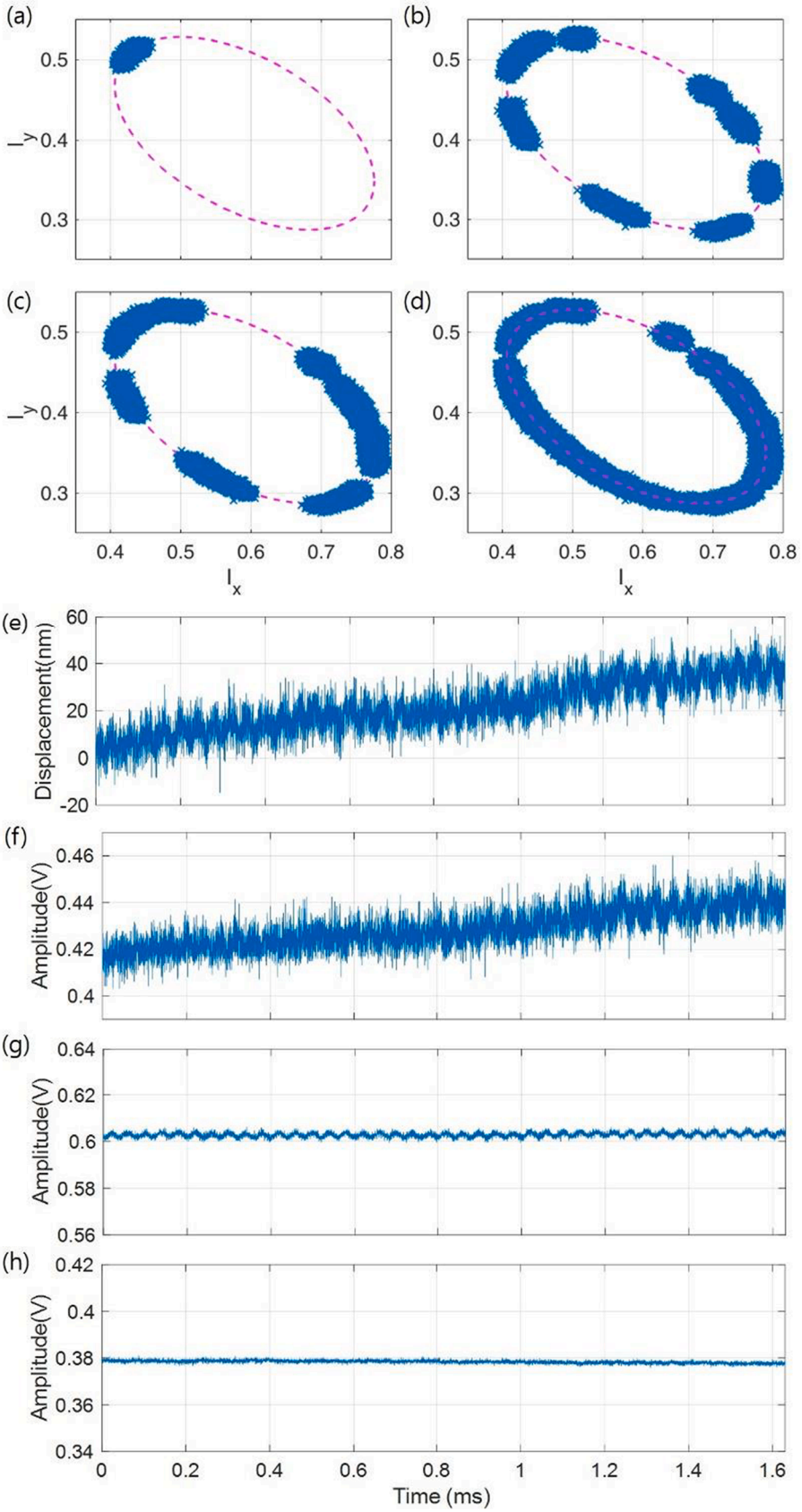

Fig. 3. Multiple measurements of a small sinusoidally oscillating displacement. Lissajous curves plotted with 1 (a), 10 (b), 20 (c), and 50 (d) data sets. (e) Time sequential displacement signal extracted from one data set of (a). (f) Channel signal I_x of (a). The channel signal directly averaged with 50 data sets of (d) for I_x (g) and I_y (h). The input was a 25 kHz sinusoidal displacement in the sample arm. Each data set was captured during a 1.632 ms time period. The time interval between nearby data sets was 1 s.

same measurement multiple times, without any intentional manipulation or specific calibration. Furthermore, by using the ellipse parameters, obtained with the multiple measurements of Fig. 3(d), the displacements of Fig. 3(a) were calculated. Fig. 3(e) shows that the displacement signal extracted from one data set is highly noisy even to figure out the 25 kHz sinusoidal behavior of the input signal. Further, we can see the signal was drifted with time. Even though the signal amplitude itself was about 16 nm, the DC level of the signal was drifted about 37 nm within 1.632 ms. Therefore, we can say that the main cause of the cocoon shape data bunch in Fig. 3(a) was caused mainly by the slow drift of the system, overwhelming the small amplitude of the applied fast displacement.

For further analysis, the time sequential signal of the first detector channel I_x in Fig. 3 (a) is plotted over the 1.632 ms time period in Fig. 3 (f). It is highly noisy also and drifting similar to Fig. 3(e). In an attempt to sharpen the signal or reduce the noise level, 50 sets of data in Fig. 3(d) were averaged directly channel by channel. Unfortunately, it was observed that the direct averaging in each detector channel was not effective as shown in Fig. 3(g) for I_x and Fig. 3(h) for I_y. They failed even showing the oscillating behavior of the 25 kHz input signal. The problem in the channel averaging is solved by utilizing the coherent average, as will be addressed in the next section. It is noted that the slow drifting in Fig. 3(f) was random in the amplitude and direction, which was nullified by averaging. Thus, Fig. 3(g) and (h) do not show appreciable drifting behavior anymore.

2.4. Coherent average

Fig. 4 shows the coherent average performed with the 50 data sets acquired for Fig. 3(d). As it was discussed, the data bunches were distributed along a closed curve, and the curve was well fitted with an ellipse. The fitting to the ellipse can be transformed to the fitting to a circle. The cosine and sine of the phase angle in Eqs. (1) and (2) can be obtained with the parameters of the ellipse fitted with 50 data sets as [15]

$$cos\phi = \frac{I_x - h}{a} \tag{4}$$

$$sin\phi = \frac{b(I_x - h)cos\delta - a(I_y - k)}{absin\delta} \tag{5}$$

Fig. 4(a) shows that the 50 data bunches transformed from the characteristic ellipse to a circle were scattered all around the circle using Eqs. (4) and (5). As shown in Fig. 4(b), we can see that one bunch of data looked like a silk cocoon, a rather fat and long one. In order to do the coherent average, the overall phase of the data points in each data bunch was calculated. Finally, the overall phases of all 50 sets were adjusted to be matched with each other. Fig. 4(c) shows the overlap of 50 data bunches after matching the overall phases. It looks much fatter than the single bunch in Fig. 4(b), even though the length is similar. However, the averaging of the overlapped data bunches gave a much thinner and shorter cocoon shape as in Fig. 4(d). Fig. 4(e) shows the displacement

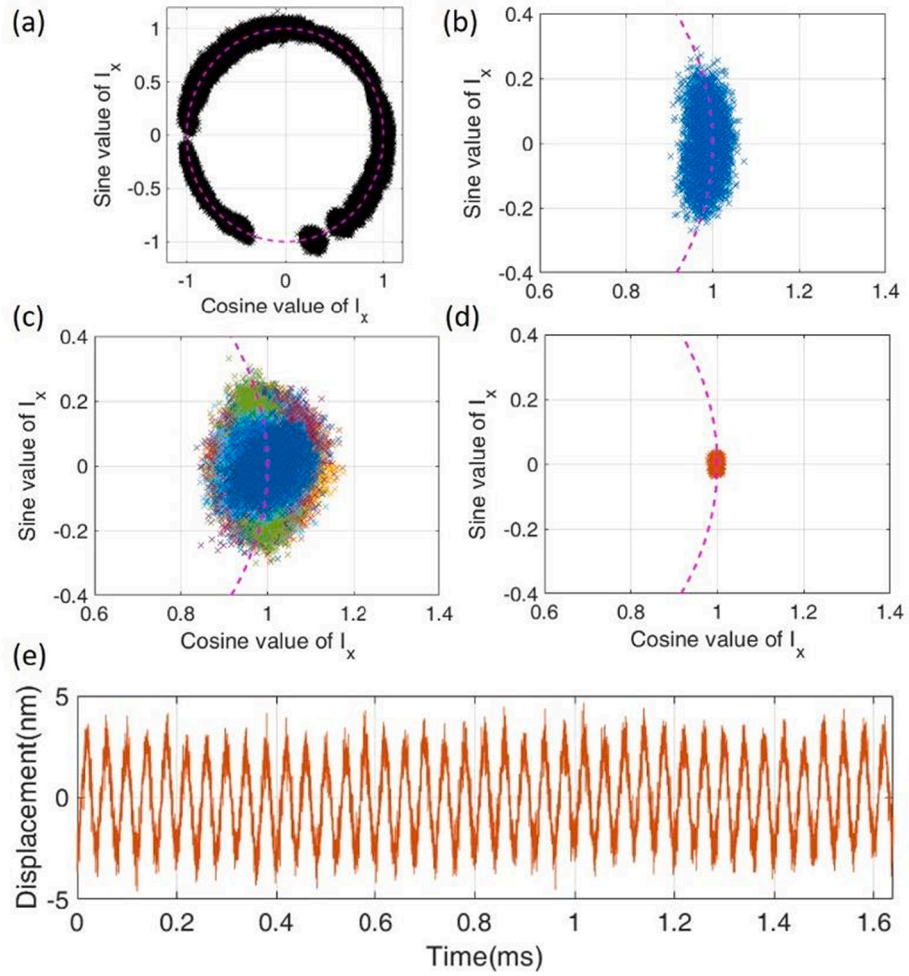

Fig. 4. The effect of coherent averaging. (a) Lissajous curve for 50 data sets transformed from characteristic ellipse to a circle. (b) Plot of just one data bunch. (c) Co-plot of 50 data bunches after matching the overall phases. (d) Plot of coherently averaged 50 data bunches. (e) The extracted time trace of coherently averaged displacements.

extracted with the coherently averaged phase angle of Fig. 4(d). We can clearly see the 25 kHz sinusoidal signal of about a 7 nm peak-to-peak amplitude, much smaller than the maximum signal range of Fig. 3(e). The length of the final cocoon in Fig. 4(d) after coherent averaging is mainly due to the amplitude of the applied signal.

The extracted displacement, without utilizing any average, was the sum of the wanted input displacement signal Δz and the unwanted initial phase ϕ_0 of the system. With Fig. 3(e), we already confirmed that the long length of the cocoon in Fig. 3(a) was mainly due to the drifting of ϕ_0. On the other hand, in Fig. 4(d), we can see that the 50 averaged cocoon became short, which means the drifting of ϕ_0 was averaged out, while the desired signal Δz was properly averaged. We can see in Fig. 4 (e) that the extracted displacement has negligible drifting.

Therefore, we can conclude that using multiple datasets offers three advantages: First, there is no need to attach any additional PZT to the reference arm to obtain the ellipse parameters for each change in the sample arm. Second, the ellipse parameters can be obtained by collecting multiple fractions of displacements smaller than $\pi/4$ each in phase. Lastly, through coherent averaging, we can reduce the system noise and nullify the effect of drifting of the system.

3. Experiment

Equipped with these verifications, we have tried to measure the thickness variation of a cornea phantom as a function of the intraocular pressure change [19,20]. As the phantom, a film of Polydimethylsiloxane (PDMS) having an air chamber underneath was prepared. Experimentally, it was found that the displacement induced by the ultrasound echo waves of LUS on the film surface was so tiny that averaging was necessary to see the thickness variation. Further, due to the pressure changes, the curvature of the PDMS film was changed, altering the characteristic ellipse of the system through deviating the reflection angle.

3.1. Sample preparation

A cornea phantom was made by attaching a PDMS film on a PDMS block with an air gap, as illustrated in Fig. 5. At first, the bottom block for the air chamber was made by pouring 10:1 PDMS mixture (silicon and curing agent) in a petri dish having a mask of 2 to 3 mm thickness. Then, to increase the absorption of excitation laser, the PDMS film was fabricated with the same PDMS mixture but adding some carbon black powders (processes 1 and 2). The thickness of the film ranged from approximately 2 to 2.5 mm. After curing, the mask was removed and a hole of 0.3 mm diameter was drilled for the pressure application at the PDMS block (process 3). Finally, the PDMS film was attached on top of the PDMS block with the O_2 plasma method (process 4). The chamber pressure was controlled using a syringe pump equipped with a pressure gauge. No noticeable leakage of air pressure was observed.

A pulse of an ultrasound wave was generated on the top surface of the PDMS film by irradiating an Nd:YAG laser pulse of a 532 nm wavelength (Brilliant Ultra 50, Quantel, France). The minute displacements on the film surface, induced by the LUS and its echoes bouncing back and forth between the top and bottom surfaces of the film, were measured over time using the proposed optical interferometric system.

3.2. Experimental setup

The basic setup was the same as Fig. 1. However, the object causing the displacement in the sample arm was changed, from PZT to a cornea phantom as shown with Fig. 6. The two interference signals were measured and digitized with a maximum 125 MS/s. For the LUS generation, an Nd:YAG laser operating at a repetition rate of 20 Hz was employed. The laser pulse was guided with a multimode fiber and collimated to the phantom with a diameter of about 5 mm. At each chamber pressure, the time sequence of surface displacements induced by a single excitation pulse was acquired as a single dataset. In order to decrease the noise level, coherent average was made with maximum 50 sets of data. With time of a round trip between nearby echo peaks, the thickness of the PDMS film was calculated. By doing the same measurement after changing the pressure, the pressure-induced thickness variation in the cornea phantom was calculated.

4. Experimental result

The LUS-induced displacements of the top surface of the PDMS film were measured under three different chamber pressures: 10 kPa, 15 kPa, and 20 kPa. Fig. 7(a) shows the Lissajous curve plotted with a single data set acquired at 10 kPa using just one excitation pulse. The time sequential displacements, of a 32.76 μs time period, extracted from Fig. 7(a) are plotted at Fig. 7(b). Unfortunately, the noise was significant to figure out the behavior of the echo signal, especially the echo peaks were not clearly distinguished. Therefore, the coherent average was made with increasing the number of data sets; 10 sets for Fig. 7(c) and (d), 30 sets for Fig. 7(e) and (f), and 50 sets for Fig. 7(g) and (h).

In the case of the single data set without averaging, the root mean square (RMS) noise equivalent displacement was calculated to be 1.23 nm. However, after performing the coherent averaging with 30 and 50 sets, the RMS noise equivalent was decreased down to 0.188 nm and 0.14 nm, respectively. We can see that the noise level becomes low enough to figure out the multiple echo peaks, induced by the ultrasound wave, of nanometer amplitudes. Interestingly, we can also see that the data bunches are rather evenly distributed along an ellipse, which is thought due to thermal expansion of the sample surface, induced by the excitation laser. It is noted that the RMS noise equivalent was calculated with the data within the time segment of 18 ~ 21 μs, but other segments gave the similar results. The equivalent displacement was decreased rapidly with the number of data sets for around the first ten and then slowly decreased. With 70 and 100 data sets, it was measured as low as 0.12 nm and 0.1 nm, respectively. However, by considering the long data acquisition time, we have used 50 as the maximum data sets for the coherent averaging.

The recurrence of the displacement signal in Fig. 7 was attributed to

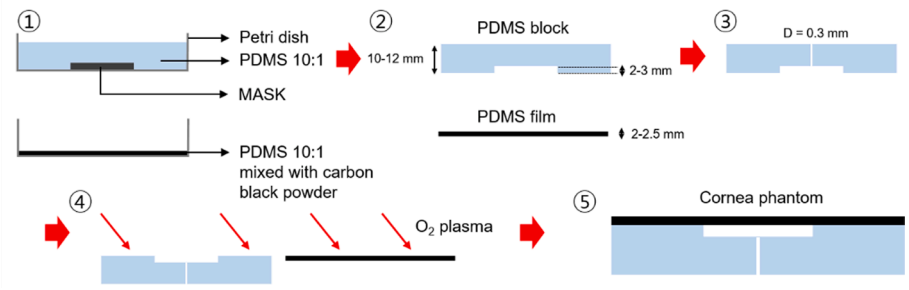

Fig. 5. The process of fabricating a cornea phantom.

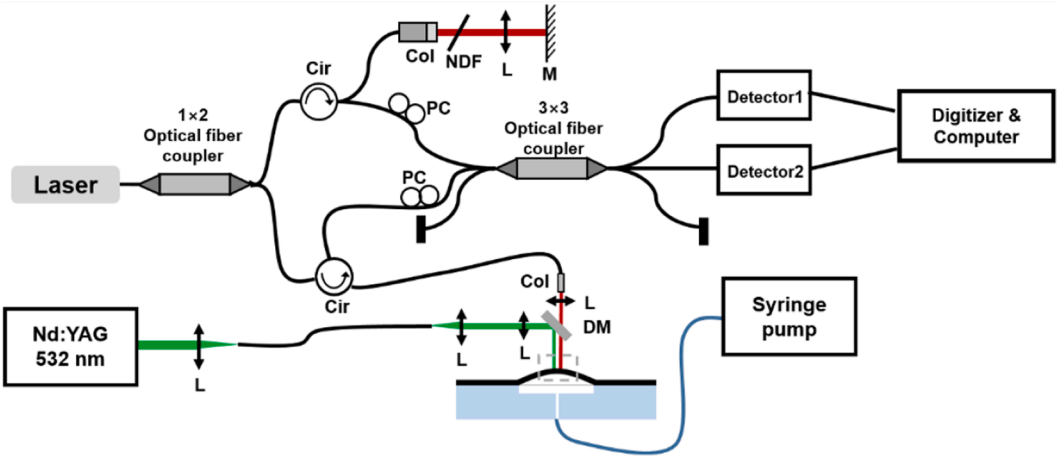

Fig. 6. Schematic of the system for measuring the time sequential small displacements caused by LUS on the surface of a cornea phantom. Cir: circulator, PC: polarization controller, L: lens, Col: collimator, NDF: neutral density filter, M: mirror, DM: dichroic mirror.

the multiple reflections of the ultrasound wave at both surfaces of the PDMS film. The ultrasound wave generated by LUS was reflected first at the bottom surface of the film, interfacing with the air-filled interior chamber, and then at the top surface of the film. The back and forth bouncing of the ultrasound wave generated the multiple echo peaks. Of course, we can see that as the number of bounces increases, the signal intensity decreases. It can be seen that the maximum peak-to-peak displacement of the echo peaks between 4.63 μs and 5.12 μs was approximately 5.78 nm and the minimum one between 30.34 μs and 30.86 μs was 1.67 nm.

The same measurements were made at other pressures also. Fig. 8 shows the three characteristic ellipses fitted with 50 data sets each but at different pressures; 10 kPa for (a), 15 kPa for (b), and 20 kPa for (c). Even though the data bunches were rather uniformly distributed along the characteristic ellipses at all pressures, the ellipses varied with pressure as can be seen in Fig. 8(d). As mentioned earlier, it is thought that the chamber pressure deformed the curvature of the PDMS film surface, so that the intensity of the beam back-coupled to the interferometer was changed with the pressure, altering the ellipse fitting parameters. Fig. 8 (d) shows that there were significant changes in the ellipse parameters due to the change in the pressure. For this reason, the ellipse parameters were calculated at each pressure first, and then the displacements were extracted with the corresponding parameters.

The time sequential echo signals measured at three different pressures, with the coherent average of 50 data sets, are plotted together in Fig. 9(a). The figure clearly shows that the arrival time of each echo peak was shortened with increasing pressure, meaning the film was thinned. The detail arrival times of all peaks are plotted in Fig. 9(b) and summarized in Table 2. Considering the ultrasound velocity of 1076 m/s in the 10:1 PDMS medium, the film thickness and its variation can be calculated with the time duration between nearby peaks [21].

For a more precise measurement of the thickness variation, the slope of the line connecting the peaks in Fig. 9(b) was calculated. As a result, we got the thickness of the film as 2.260 mm at 10 kPa, 2.211 mm at 15 kPa, and 2.152 mm at 20 kPa, giving about 10.8 μm/kPa as the thickness reduction rate. The resolution of the thickness measurement is determined by the sampling rate and the speed of ultrasound in the medium. Considering the digitizer's sampling rate of 125 MS/s and the ultrasound velocity of 1076 m/s in PDMS, we can estimate the resolution of 4.3 μm. Of course, this can be enhanced further by increasing the digitizer's sampling rate.

Even though the experiment with real human eyes could not be performed in this work, we proposed a new method for measuring ocular pressure without any irritating physical contact or uncomfortable air puffing on eyes.

5. Discussions

As confirmed by the experimental results, the proposed system successfully measured the surface displacements induced by the ultrasound wave of LUS. Without using additional devices or equipment, the minute displacements could be acquired even when the amount of reflection in the sample arm was changed during the measurement.

The proposed method has two main advantages. First, in a conventional 3 × 3 interferometric system, the ellipse parameters are calculated or extracted before the main measurements, usually by adding a PZT to the reference arm. However, in the situation where line or area scan is required, the PZT must be driven at every measuring points, making the system complicated and increasing the process time. Whilst, the proposed method can obtain the ad hoc characteristic ellipse of the system by using multiple data sets acquired at a point. Second, when the displacements under measurement are small, it is difficult to accurately distinguish between noise and the signal using only one data set. However, by acquiring multiple data sets at a point over a period of time, we can perform the coherent average, which allows us to measure the time varying displacement signals of even sub-nanometer amplitudes.

The proposed method can be applied to the fields where ultrasound is involved. For example, we can think of preventing GIS (gas-insulated switchgear) failure by monitoring the ultrasonic waves generated by electric discharge. A GIS system switches high voltage electric power lines. In general, unwanted electric discharge frequently occurs between the conductor to which high voltage is applied and the housing surrounding the conductor [22]. By monitoring the ultrasonic waves outside or on the housing at an early stage of partial discharge, we can reduce the failure or break down risk of the GIS system.

6. Conclusion

Experimentally, it was observed that the characteristic ellipse of a 3 × 3 optical interferometer was easily affected by changes in the sample arm, such as by lateral scanning and curvature variation of the specimen surface. Fortunately, the characteristic ellipse could be reconstructed using the multiple data sets captured for coherent averaging. The troublesome drift of the initial phase of the system could be used to obtain the ad hoc characteristic ellipse of the system.

Based on this method, we have presented the method that could measure the time-sequential minute displacements caused by the ultrasound waves of LUS. An optical interferometer based on a 3 × 3 optical fiber coupler was utilized to measure the time-varying displacement of a cornea-mimicking phantom surface without physical contact. Due to the intrinsic phase shift of the 3 × 3 interferometer,

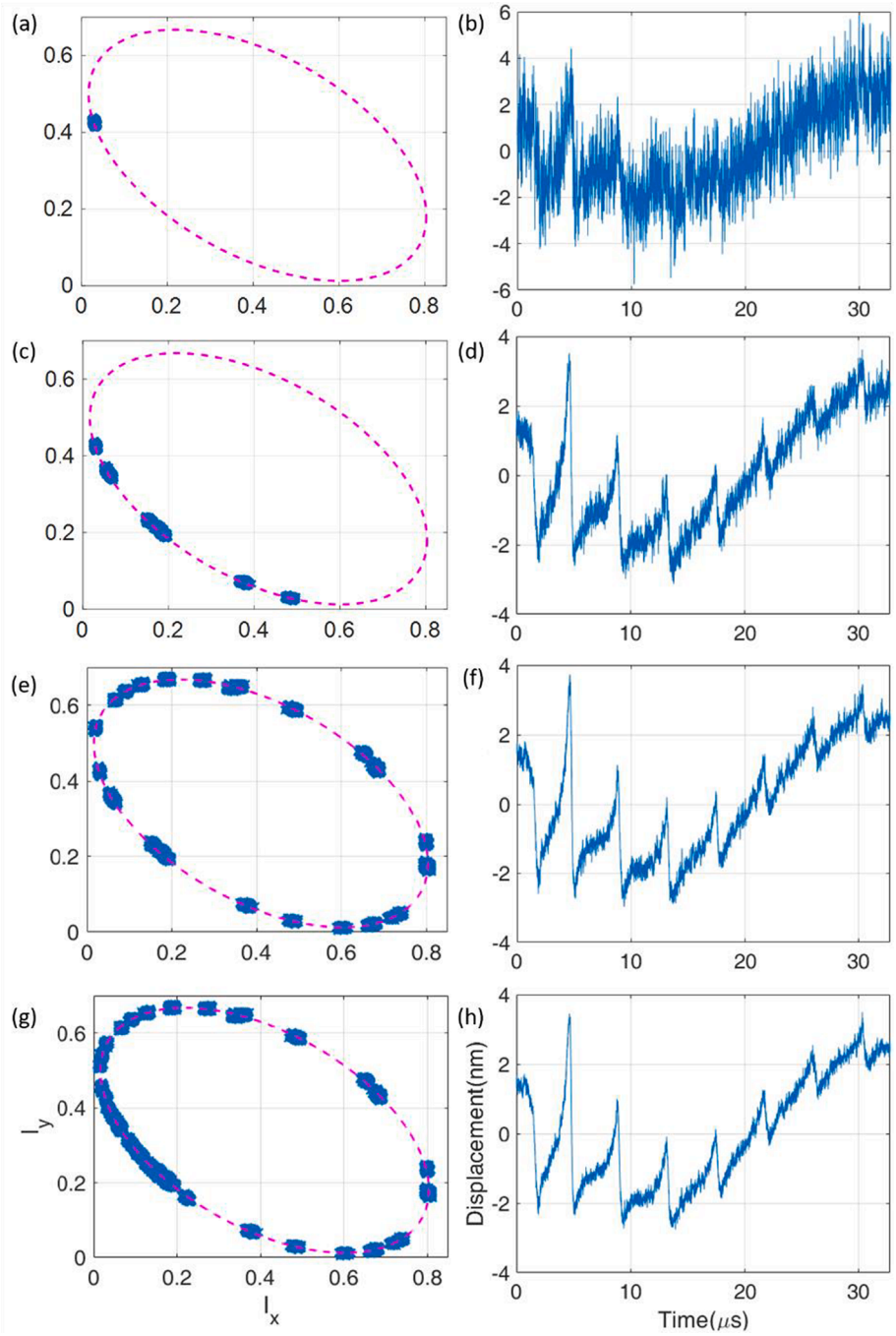

Fig. 7. The Lissajous curves (left column) and the corresponding coherent averaged time sequential displacements (right column) extracted with 1 data set (a)(b), 10 sets (c)(d), 30 sets (e)(f), and 50 sets (g)(h). Each data set is the time sequential echo signal for a single excitation pulse operating at a repetition of 20 Hz. The red dotted curve is the common characteristic ellipse expected for the cornea phantom under 10 kPa pressure.

initial phase or operating point-insensitive measurements could be implemented. By performing coherent averaging, the RMS noise equivalent displacement could be reduced down to 0.14 nm. Finally, by using the time of a round trip between the LUS echo peak signals, the ocular pressure-induced thickness variation of the cornea phantom was measured to be 10.8 μm/kPa. As a result, the time varying displacements of sub-nanometer amplitudes generated by ultrasound waves of LUS were successfully measured. It is expected that the proposed system will find interesting applications in various fields where ultrasound is involved, such as GIS.

Ethical approval

This article does not contain any studies with human participants or animals performed by any of the authors.

Informed consent

There are no individual participants included in the study.

Funding

This work was supported by the Technology Innovation Program

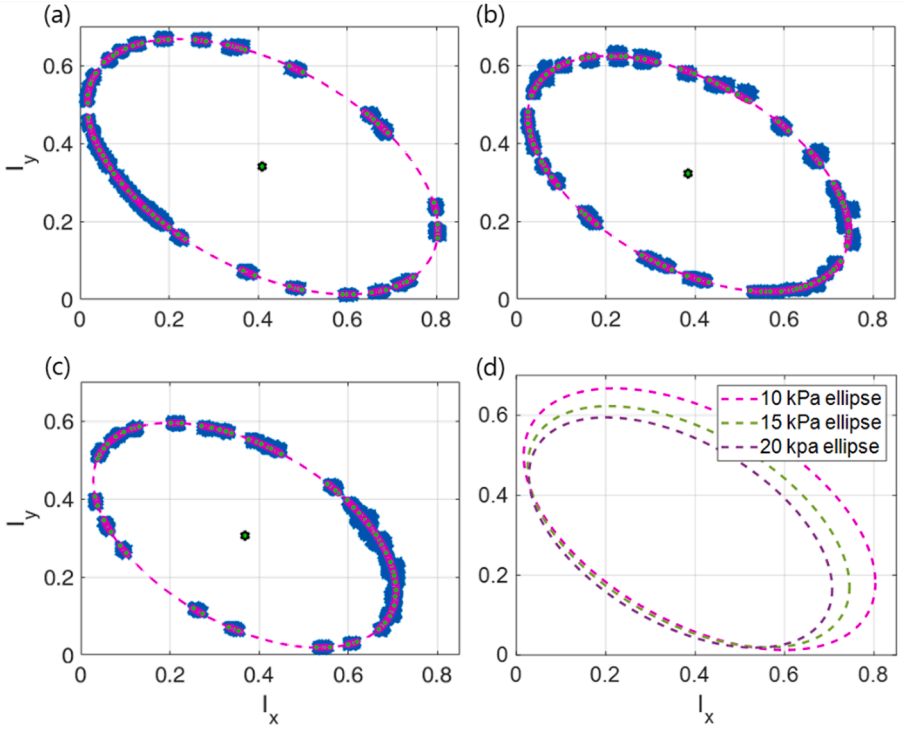

Fig. 8. The Lissajous curves plotted for different pressures; (a) 10 kPa, (b) 15 kPa, and (c) 20 kPa. (d) Co-plot of the characteristic ellipses.

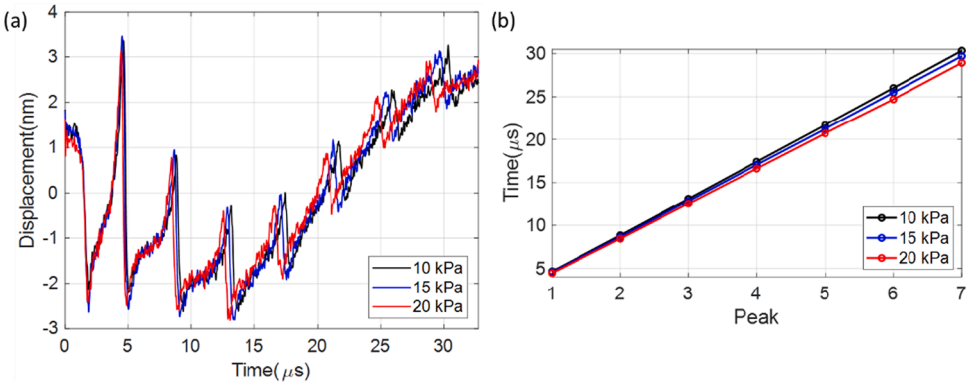

Fig. 9. The coherent averaged echo signals of the cornea phantom. (a) The time sequential displacement signals measured at pressures of 10 (black), 15 (blue), and 20 (red) kPa. (b) The co-plot of arriving times of all echo peaks. The coherent average was made with 50 data sets at each pressure.

Table 2
Arriving time of each echo peak in Fig. 9 (Unit in μs).

Pressure Peak #	10 kPa	15 kPa	20 kPa
1	4.63	4.55	4.45
2	8.83	8.66	8.45
3	13.11	12.84	12.53
4	17.42	17.07	16.63
5	21.70	21.24	20.72
6	26.02	25.48	24.70
7	30.34	29.71	28.94

(20021979, Development of health monitoring system for gas insulated switchgears by using optical sensing modalities) funded by the Ministry of Trade, Industry and Energy (MOTIE, Republic of Korea) and GIST Research Project grant funded by GIST in 2024.

CRediT authorship contribution statement

Younggue Kim: Writing – original draft, Software, Investigation, Formal analysis, Data curation, Conceptualization. **Taeil Yoon:** Writing – review & editing, Validation, Software, Conceptualization. **Byeongha Lee:** Writing – review & editing, Validation, Supervision, Project administration, Funding acquisition, Conceptualization.

Declaration of competing interest

The authors declare that they have no known competing financial interests or personal relationships that could have appeared to influence the work reported in this paper.

Data availability

Data will be made available on request.

References

[1] J.-D. Aussel, J.-P. Monchalin, Precision laser-ultrasonic velocity measurement and elastic constant determination, Ultrasonics 27 (1989) 165–177, https://doi.org/10.1016/0041-624X(89)90059-0.

[2] A. Cavuto, M. Martarelli, G. Pandarese, G.M. Revel, E.P. Tomasini, Train wheel diagnostics by laser ultrasonics, Measurement 80 (2016) 99–107, https://doi.org/10.1016/j.measurement.2015.11.014.

[3] R.E. Green, Non-contact ultrasonic techniques, Ultrasonics 42 (2004) 9–16, https://doi.org/10.1016/j.ultras.2004.01.101.

[4] C.B. Scruby, Some applications of laser ultrasound, Ultrasonics 27 (1989) 195–209, https://doi.org/10.1016/0041-624X(89)90043-7.

[5] I. Pelivanov, T. Buma, J. Xia, C.-W. Wei, M. O'Donnell, A new fiber-optic non-contact compact laser-ultrasound scanner for fast non-destructive testing and evaluation of aircraft composites, J. Appl. Phys. 115 (2014) 113105, https://doi.org/10.1063/1.4868463.

[6] J.B. Hoyes, Q. Shan, R.J. Dewhurst, A non-contact scanning system for laser ultrasonic defect imaging, Meas. Sci. Technol. 2 (1991) 628–634, https://doi.org/10.1088/0957-0233/2/7/009.

[7] S.J. Davies, C. Edwards, G.S. Taylor, S.B. Palmer, Laser-generated ultrasound: its properties, mechanisms and multifarious applications, J. Phys. D: Appl. Phys. 26 (1993) 329–348, https://doi.org/10.1088/0022-3727/26/3/001.

[8] F. Sun, J. Chen, J. Zhang, X. Chen, K. Jia, L. Fan, X. Xu, L. Cheng, X. Yan, S. Zhang, Study on the surface/subsurface defects of cylindrical components based on laser ultrasonic technology, Opt. Laser Technol. 180 (2025) 111399, https://doi.org/10.1016/j.optlastec.2024.111399.

[9] P.L.M. Heydemann, Determination and correction of quadrature fringe measurement errors in interferometers, Appl. Opt., AO 20 (1981) 3382–3384. doi: 10.1364/AO.20.003382.

[10] S. Rerucha, Z. Buchta, M. Sarbort, J. Lazar, O. Cip, Detection of interference phase by digital computation of quadrature signals in homodyne laser interferometry, Sensors 12 (2012) 14095–14112, https://doi.org/10.3390/s121014095.

[11] S. Zhang, S. Zhang, Y. Tan, L. Sun, Self-mixing interferometry with mutual independent orthogonal polarized light, Opt. Lett. 41 (2016) 844, https://doi.org/10.1364/OL.41.000844.

[12] P. Gregorčič, T. Požar, J. Možina, Quadrature phase-shift error analysis using a homodyne laser interferometer, Opt. Express 17 (2009) 16322, https://doi.org/10.1364/OE.17.016322.

[13] F. Xie, J. Ren, Z. Chen, Q. Feng, Vibration-displacement measurements with a highly stabilised optical fiber Michelson interferometer system, Opt. Laser Technol. 42 (2010) 208–213, https://doi.org/10.1016/j.optlastec.2009.06.010.

[14] A.T. Hoang, T.T. Vu, D.Q. Pham, T.T. Vu, T.D. Nguyen, V.H. Tran, High precision displacement measuring interferometer based on the active modulation index control method, Measurement 214 (2023) 112819, https://doi.org/10.1016/j.measurement.2023.112819.

[15] S. Park, J. Lee, Y. Kim, B.H. Lee, Nanometer-scale vibration measurement using an optical quadrature interferometer based on 3 × 3 fiber-optic coupler, Sensors 20 (2020) 2665, https://doi.org/10.3390/s20092665.

[16] M. Kim, B. Cho, H. Lee, T. Yoon, B. Lee, Implementation of hemispherical resonator gyroscope with 3 × 3 optical interferometers for analysis of resonator asymmetry, Sensors 22 (2022) 1971, https://doi.org/10.3390/s22051971.

[17] T. Yoon, Y. Kim, M. Awais, B. Lee, Acoustic velocity measurement for enhancing laser ultrasound imaging based on time domain synthetic aperture focusing technique, Sensors 23 (2023) 2635, https://doi.org/10.3390/s23052635.

[18] S. Gu, G. Zhang, Q. Ge, L. Xu, X. Wu, B. Yu, Ameliorated 3 × 3 coupler-based demodulation algorithm using iteratively reweighted ellipse specific fitting, Opt. Express 32 (2024) 1108, https://doi.org/10.1364/OE.501258.

[19] L.W. Herndon, Measuring intraocular pressure-adjustments for corneal thickness and new technologies, Curr. Opin. Ophthalmol. 17 (2006) 115–119, https://doi.org/10.1097/01.icu.0000193093.05927.a1.

[20] A. Kotecha, A. Elsheikh, C.R. Roberts, H. Zhu, D.F. Garway-Heath, Corneal thickness- and age-related biomechanical properties of the cornea measured with the ocular response analyzer, Invest. Ophthalmol. Vis. Sci. 47 (2006) 5337, https://doi.org/10.1167/iovs.06-0557.

[21] J.K. Tsou, J. Liu, A.I. Barakat, M.F. Insana, Role of ultrasonic shear rate estimation errors in assessing inflammatory response and vascular risk, Ultrasound Med. Biol. 34 (2008) 963–972, https://doi.org/10.1016/j.ultrasmedbio.2007.11.010.

[22] G.-M. Ma, H. Zhou, M. Zhang, C.-R. Li, Y. Yin, Y.-Y. Wu, A high sensitivity optical fiber sensor for GIS partial discharge detection, IEEE Sensors J. 19 (2019) 9235–9243, https://doi.org/10.1109/JSEN.2019.2925848.